J. Fluid Mech. (2023), *vol*. 954, A19, doi:10.1017/jfm.2022.967

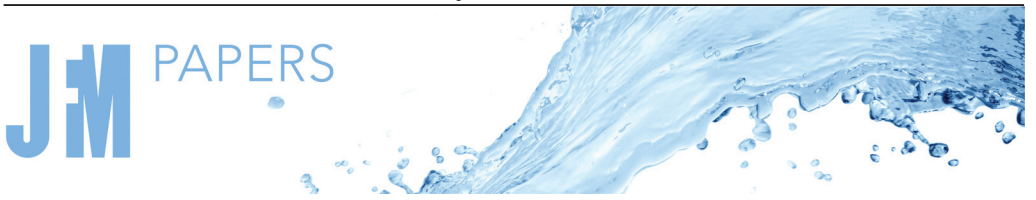

Nonlinear wave attenuation in strongly confined falling liquid films sheared by a laminar counter-current gas flow

Sophie Mergui[1,2,†], Gianluca Lavalle[3], Yiqin Li[1], Nicolas Grenier[4] and Georg F. Dietze[1]

[1]Université Paris-Saclay, CNRS, FAST, 91405 Orsay, France

[2]Sorbonne Université, UFR 919, 4 place Jussieu, F-75252 Paris CEDEX 05, France

[3]Mines Saint-Etienne, Université Lyon, CNRS, UMR 5307 LGF, Centre SPIN, F-42023 Saint-Etienne, France

[4]Université Paris-Saclay, CNRS, LISN, 91405 Orsay, France

(Received 27 April 2022; revised 12 October 2022; accepted 7 November 2022)

Experiments are conducted in water films falling along the bottom wall of a weakly inclined rectangular channel of height 5 mm in the presence of a laminar counter-current air flow. Boundary conditions have been specifically designed to avoid flooding at the liquid outlet, thus allowing us to focus on the wave dynamics in the core of the channel. Surface waves are excited via coherent inlet forcing before they come into contact with the air flow. The effect of the air flow on the height, shape and speed of two-dimensional travelling nonlinear waves is investigated and contrasted with experiments of Kofman, Mergui & Ruyer-Quil (*Intl J. Multiphase Flow*, vol. 95, 2017, pp. 22–34), which were performed in a weakly confined channel. We observe a striking difference between these two cases. In our strongly confined configuration, a monotonic stabilizing effect or a non-monotonic trend (i.e. the wave height first increases and then diminishes upon increasing the gas flow rate) is observed, in contrast to the weakly confined configuration where the gas flow is always destabilizing. This stabilizing effect implies the possibility of attenuating waves via the gas flow and it confirms recent numerical results obtained by Lavalle *et al.* (*J. Fluid Mech.*, vol. 919, 2021, R2) in a superconfined channel.

Key words: thin films, gas/liquid flow, solitary waves

† Email address for correspondence: sophie.mergui@sorbonne-universite.fr

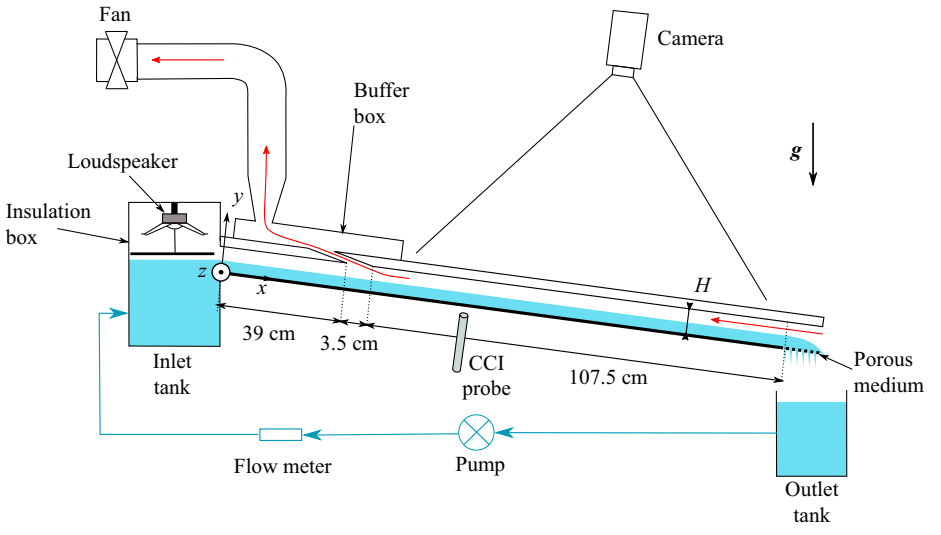

Figure 1. Sketch of the experimental set-up. The liquid loop appears in blue and the gas path is highlighted by a red arrows in the channel gap.

1. Introduction

We consider a falling liquid film in contact with a laminar counter-current gas flow within a narrow rectangular channel inclined at an angle β (figure 1). This configuration can be considered as a prototype for compact devices found in engineering applications, such as reflux condensers and distillation columns with structured packings (Valluri *et al.* 2005). It is well known that the interaction between the wavy film and the gas flow can promote flooding events leading to a deterioration in the process performance. Depending on the geometry and/or ratio of liquid and gas flow rates (or superficial velocities), we can observe film atomization (Zapke & Kröger 2000), wave or liquid flow reversal (Tseluiko & Kalliadasis 2011) or obstruction of the channel (Vlachos *et al.* 2001). In order to prevent or delay such events, it is crucial to characterize the dynamics of interfacial waves and in particular their linear and nonlinear responses to the gas flow.

Many theoretical and experimental works dedicated to the linear stability of falling films are reported in the literature since the seminal work of Kapitza (1948) on the different wavy flow regimes. The linear stability analysis of a liquid film in a passive atmosphere was initiated by Benjamin (1957) and Yih (1963). They found that the film is unstable to long-wave disturbances when the Reynolds number is greater than $5/6 \cot \beta$ through an inertia-driven mechanism. This threshold for the so-called Kapitza instability was confirmed experimentally by Liu, Paul & Gollub (1993). Recent theoretical investigations (Lavalle *et al.* 2019) have shown that the impact of the gas phase on the linear stability threshold becomes non-negligible in weakly inclined and/or strongly confined channels by causing a stabilizing effect and ultimately the full suppression of the Kapitza instability. This linear stabilization due to confinement was confirmed experimentally in Lavalle *et al.* (2019) for a water film in contact with quiescent air in a slightly inclined channel ($\beta = 1.69°$) of height $H = 5$ mm. The main ingredient involved in the stabilization mechanism was found to be the tangential viscous stress exerted by the gas on the film surface, as suggested by Tilley, Davis & Bankoff (1994). The strong stabilizing effect induced by a counter-current air flow on a wavy water film is reproduced by Trifonov (2019) at small inclination and strong confinement. Kushnir *et al.* (2021), via a comprehensive parametric

study, have recently established that regimes of linear stabilization in the case of a zero net gas flow occur for channel heights $H \leqslant 10$ mm at $\beta = 1^\circ$ and $H \leqslant 2$ mm at $\beta = 10^\circ$ in a water–air system.

Furthermore, when the gas flows in a counter-current fashion, it was shown in Lavalle *et al.* (2019) that the linear stabilization is intensified over the entire range of unstable wavenumbers when the confinement is sufficiently strong. For intermediate confinement levels, the linear effect of the gas flow can become non-monotonic, i.e. the cutoff wavenumber of the Kapitza instability first decreases and then increases with the gas flow rate (Vellingiri, Tseluiko & Kalliadasis 2015; Trifonov 2017; Lavalle *et al.* 2019). The stabilizing effect observed at low gas flow rate arises at all wavenumbers. By contrast, when the gas flow rate is large, short waves are attenuated while long waves are amplified, in accordance with the experiments of Alekseenko *et al.* (2009) and Vellingiri *et al.* (2015) on linear waves in a vertically falling liquid film, which were conducted in a vertical tube with a turbulent counter-current gas flow. Finally, for weak confinement, a monotonic increase of the cutoff wavenumber is observed and the destabilization of the film arises at all wavenumbers.

The nonlinear response of surface waves has also been studied in a number of works, usually involving a turbulent counter-current gas flow in the context of flooding (Vlachos *et al.* 2001; Drosos, Paras & Karabelas 2006; Trifonov 2010; Tseluiko & Kalliadasis 2011; Kofman, Mergui & Ruyer-Quil 2017). These studies, which concerned weak confinement levels or vertical configurations, revealed that the amplitude of nonlinear waves increases and steepens with increasing gas flow rate while their speed decreases. The authors also observed that capillary ripples in front of the solitary waves are damped, in line with the linear stabilization of short waves observed by Alekseenko *et al.* (2009). In the weakly confined setting, flooding manifests itself in experiments as wave reversal or wave breaking phenomena (Drosos *et al.* 2006; Kofman *et al.* 2017) emerging from the interfacial shear stress imposed by the gas flow. By contrast, in strongly confined vertical channels, flooding is usually associated with a wave-induced local obstruction of the channel cross-section (Vlachos *et al.* 2001; Dietze & Ruyer-Quil 2013), which can coincide with wave reversal events (Lavalle *et al.* 2020). In such configurations, the counter-current gas flow amplifies the wave height and thus increases the flooding risk. Recent numerical investigations suggest that this trend could be inverted in weakly inclined channels. For example, Trifonov (2019) identified a non-monotonic variation of the interfacial velocity, mean film thickness and interphase friction coefficient with increasing counter-current gas velocity, although the trend of the wave amplitude remained monotonic and increasing. Lavalle *et al.* (2021) have identified regimes where the nonlinear wave height and the linear growth rate both decrease with increasing gas flow rate. Such regimes, if confirmed experimentally, could avoid catastrophic flooding events, while exploiting the benefits of surface waves (e.g. intensification of heat and mass transfer).

The main aim of the current manuscript is to confirm the existence of such regimes through experiments. We study the effect of a counter-current laminar air flow on forced two-dimensional (2-D) solitary waves resulting from the Kapitza instability in a weakly inclined ($\beta = 4.9^\circ$) strongly confined channel of 5 mm height. A particular attention has been paid to the boundary conditions, specifically designed to avoid flooding due to outlet effects at the end of the test section, thus allowing us to focus on the wave dynamics in the core of the channel. Temporal forcing is applied at the liquid inlet to force surface waves within a buffer zone before they come into contact with the air flow. The influence of the gas shear stress on the shape, amplitude and velocity of these nonlinear waves is investigated and contrasted with the experiments of Kofman *et al.* (2017), which were

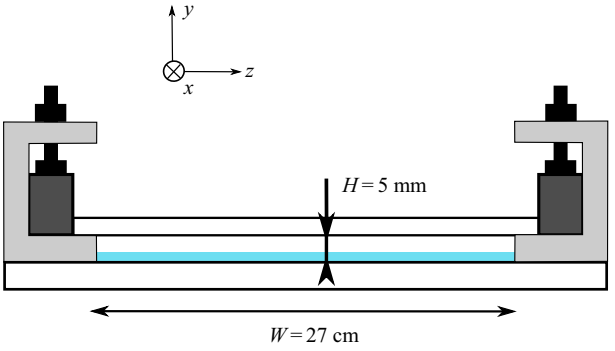

Figure 2. Sketch of the channel cross-section.

performed in a weakly confined channel ($H = 19$ mm) where the gas flow was turbulent. Furthermore, we are interested in the effect of the surface waves on the mean film thickness when the gas velocity is increased.

The paper is organized as follows. The experimental set-up and the measuring techniques are presented in § 2. Results are presented in § 3, where we discuss the response of nonlinear surface waves to an increase in counter-current gas flow rate. In § 3.1, we focus on the role of the confinement level, by contrasting our results with the weakly confined experiments of Kofman *et al.* (2017). In § 3.2, we focus on the effect of the counter-current gas flow on the dynamics of precursory capillary ripples. In § 3.3, we discuss the role of the liquid Reynolds number and finally in § 3.4 we assess the effect of surface waves on the mean film thickness. Conclusions are drawn in § 4.

2. Experimental set-up and measurement methods

A general view of the experimental apparatus is sketched in figure 1: a liquid film falling on the bottom plate of an inclined rectangular channel in contact with a counter-current gas flow. Figure 2 displays a cross-sectional view of the channel. The liquid-related part is the same as the one used in Lavalle *et al.* (2019). In § 2.1, we recall briefly its main characteristics. Then in § 2.2 we describe the part related to the gas phase.

2.1. *Liquid loop*

The liquid-related part consists of an inclined glass plate ($L = 150$ cm long, $W = 27$ cm wide and 5 mm thick) placed on a massive framework mounted on rubber feet to dampen environmental vibrations. The inclination angle β can be changed in the range 0°–20° and is measured using an inclinometer with a precision of 0.05°. In this work β is fixed to 4.9°. At the channel exit, the glass plate is extended with a porous medium that drains the liquid away, allowing us to avoid flooding events due to exit effects. A gear pump brings the liquid from the outlet tank located at the exit of the plane to an inlet tank, from which the liquid overflows and runs onto the plane. The volumetric liquid flow rate, q_l, is changed by varying the pump power and is measured by using a magnetic-induced flow meter. The liquid Reynolds number is calculated as

$$Re_l = \frac{q_l}{\nu_l W}, \tag{2.1}$$

where ν_l is the kinematic viscosity of the liquid.

In this study, Re_l is varied in the range 20–49. A temporal periodic forcing of the film is introduced at the inlet to trigger surface waves of prescribed frequency f. This is achieved through a thin aluminium plate fixed to the membrane of two loudspeakers thus generating harmonic vibrations above the liquid surface across the whole width of the inlet tank (Kofman *et al.* 2017). The choice of the forcing frequency depends on Re_l and is based on the aerostatic case (without counter-current gas flow). We adjust it such that 2-D saturated travelling waves are observed at the end of the unsheared zone while avoiding secondary subharmonic or side-band instability (Liu & Gollub 1994). The waves then form a regular wave train over the working area and appear as a large hump preceded by capillary ripples.

Water is used as working liquid. The temperature of the liquid is measured in the outlet tank and upstream of the inlet tank. The surface tension is regularly monitored by taking a water sample then using a drop shape analyser. A one-point temporal measurement of the film thickness based on the confocal chromatic imaging (CCI) technique (Cohen-Sabban, Gaillard-Groleas & Crepin 2001) is performed through the bottom glass plate with a spatial precision of 250 nm and a temporal resolution up to 2 kHz. The CCI probe is mounted on a linear translation stage in order to perform measurements along the streamwise axis of the glass plate. In this study, the film thickness is measured at the midwidth and at $x = 60$ cm from the inlet (see figure 1). An example of a CCI time trace is shown in figure 3(*a*). From such temporal measurements, we can extract the time-averaged film thickness, h_m (blue line) and the film thickness range, given by h_{max} and h_{min}, which correspond to the statistical mean of the maximum and minimum wave height values measured over the duration of the signal (red line and green line). The temporal fluctuations of h_{max} and h_{min} are quantified from the standard deviation of the statistical measurements and are used to include error bars in the relevant figures.

In addition, we can extract the local free-surface temporal slope, $\partial_t h$, and calculate the statistical mean of its maximum and minimum values over the duration of the signal, as well as the related standard deviation. Figure 3(*b*) represents a blown-up view over three wave periods, where we have highlighted the maximum (positive) and minimum (negative) free-surface slope magnitude, located at the back of the first capillary wave (square) and at the main front (upward triangle), respectively. The maximum free-surface slope magnitude is also indicated (downward triangle).

For a given liquid Reynolds number, we quantify the relative confinement of the liquid film with the global parameter

$$\eta_0 = \frac{H}{h_m^0}, \tag{2.2}$$

where h_m^0 is the time-averaged film thickness measured in the case of a quiescent gas (superscript 0), i.e. without imposing a counter-current gas flow.

In addition to the pointwise CCI film thickness measurement, we visualize the film surface with shadowgraphy. For this, the film is illuminated with an oblique white light sheet and imaged from the top either by a 2-D camera to provide shadowgraphs over whole width and length of the working area (figure 4*a*) or by a linear CCD camera focused on the central axis ($z = 0.5W$) to obtain spatiotemporal diagrams (figure 4*b*) from which the wave speed, c, is determined. At least two spatiotemporal diagrams are acquired for each experiment and we measure the velocity of several waves around $x = 60$ cm on each diagram. Then c is the mean of the set of measurements and the related error is given by corresponding the standard deviation. The wave speed can also be used to convert the temporal slope $\partial_t h$ of the film surface to the spatial slope $\partial_x h = \partial_t h/c$.

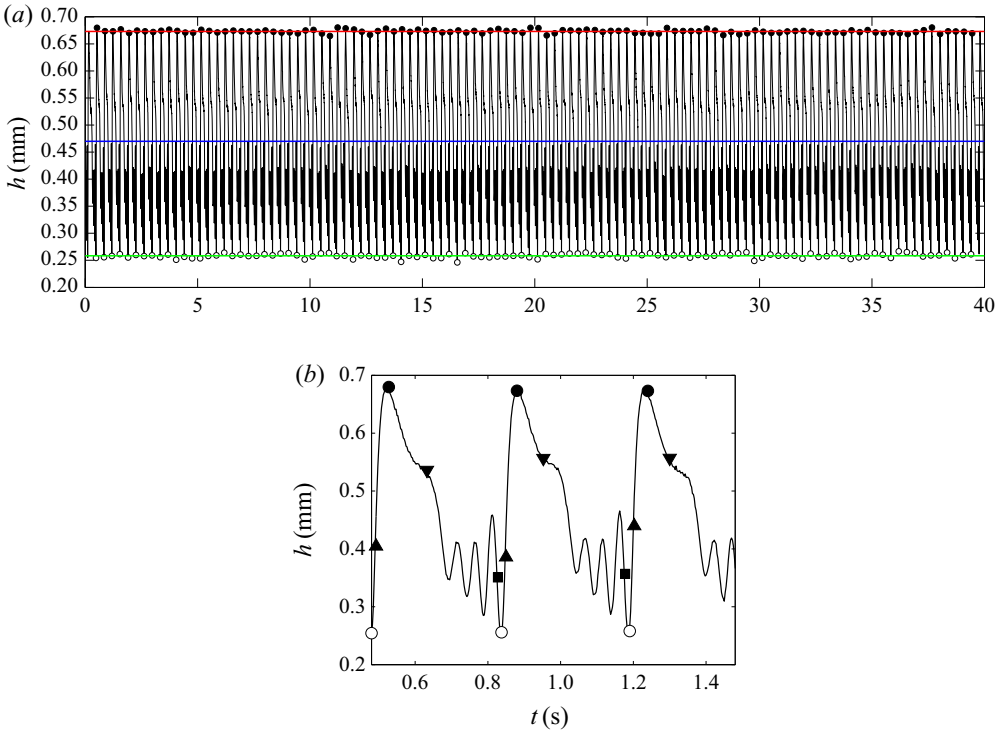

Figure 3. Film thickness time trace measured with the CCI technique. Here $Re_l = 35$, $f = 2.8$ Hz, $\eta_0 = 11.1$, without counter-current gas flow. (*a*) The blue line corresponds to the time-averaged film thickness over the duration of the signal. Open and filled circles correspond to the minimal and maximal height of each wave in the signal, respectively. (*b*) Enlargement of the signal presented in (*a*). Squares and downward triangles mark the maximum positive free-surface slope magnitude, located at the back of the first capillary wave and at the main wave tail. Upward triangles mark the maximum negative free-surface slope magnitude, located at the main wavefront.

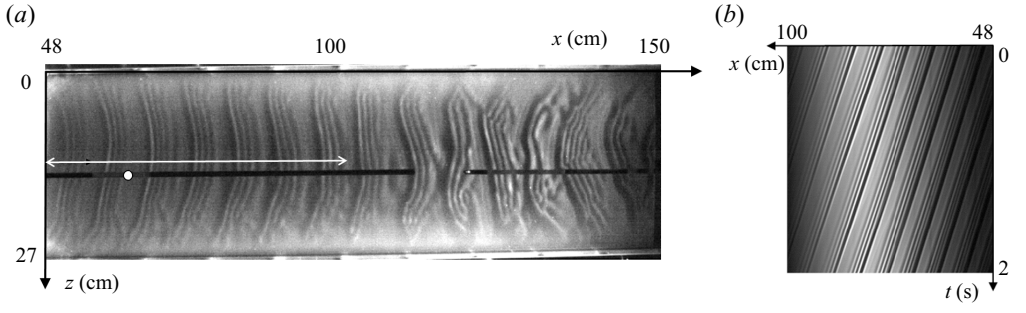

Figure 4. Typical experiment: $Re_l = 35$, $f = 2.8$ Hz, $\eta_0 = 11.1$, without counter-current gas flow (aerostatic case). (*a*) Visualization of the gas–liquid interface over the entire test section. The white arrow marks the length over which spatiotemporal diagrams are constructed. The filled white circle marks the location for the CCI measurements ($x = 60$ cm). (*b*) Spatiotemporal diagram obtained using a linear camera located in the midplane ($z = 13.5$ cm).

2.2. *Gas loop*

The gas flow is confined between the surface of the falling liquid film, which flows on the bottom glass plate, and an upper 5 mm thick glass plate placed at a distance H from the bottom one. The uniformity of H is regularly checked both in the streamwise and the transverse directions, based on measurements with the CCI method. From one experiment to another, H can vary from 5 mm to 5.2 mm depending on the force applied by the screws used to fix the top plate, but its variation for a given experiment is less than 0.5 %. Ambient air is sucked through the channel using a fan (see figure 1). The gas flow enters the channel at the lower end and leaves through an outlet slot spanning the entire width of the top plate. This slot ranges from $x = 39$ cm to $x = 42.5$ cm and opens into a buffer box to which the fan is connected via a flexible pipe. Upstream of the slot ($x < 39$ cm), the liquid film is allowed to develop without being disturbed by the gas flow.

The air flow rate, q_g, is controlled by the fan power and is quantified based on a calibration curve, which was obtained by measuring velocity profiles over the channel height with a hot-wire anemometer, at different fan powers. The procedure is detailed in Appendix A. These calibration measurements were performed in the absence of a liquid film and we define a gas Reynolds number as

$$Re_g = \frac{q_g}{\nu_g W}, \tag{2.3}$$

where ν_g is the kinematic viscosity of the gas and q_g is the gas flow rate measured in a dry channel at the same fan power.

For the range of parameters used in this study, we assume that for a given fan power, the air flow rate is not significantly affected by the presence of the liquid film in the channel and thus the Re_g values are representative of the gas flow rate in the falling liquid film experiments. This statement is discussed at the end of Appendix A.

In this paper, Re_g was varied up to 1350, beyond which flooding occurs in the channel for the liquid Reynolds number values considered. Experiments performed by Patel & Head (1969) in a rectangular channel of aspect ratio $W/H = 48$, which is comparable to the confined channel used in this paper ($W/H = 54$), showed that the flow remains laminar up to $Re_g = 1300$ and becomes fully turbulent for $Re_g > 2800$. Velocity measurements conducted in our channel and presented in Appendix A confirmed that the laminar–turbulent transition starts at $Re_g > 1200$. We can thus conclude that the gas flow is laminar in the experiments presented in this paper.

The mean gas velocity, u_g, is defined as the spatially averaged velocity over the gas cross-section and is determined from q_g as follows:

$$u_g = \frac{q_g}{W(H - h_m)}, \tag{2.4}$$

where h_m is the time-averaged film thickness measured in the presence of the counter-current gas flow, and remains almost constant along the central axis of the channel in the sheared region (i.e. downstream of the slot) for a given gas flow rate, as shown in figure 5 (filled circles). So we can consider that the mean gas velocity does not depend on the streamwise position. Figure 5 also shows that the liquid film is not affected by the counter-current gas flow in the unsheared zone upstream of the slot ($x < 39$ cm). Finally, this figure highlights the influence of the waves on the mean film thickness. We observe that the measured mean film thickness without imposed counter-current gas flow (empty circles) matches the primary-flow solution (dashed line) near the liquid inlet, then it decreases in the streamwise direction as the surface waves develop due to secondary instability.

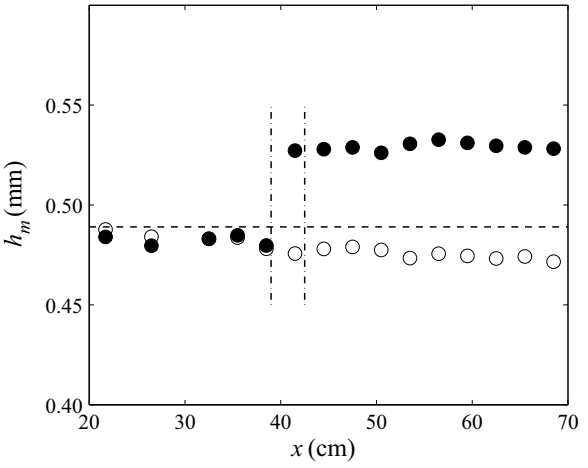

Figure 5. Streamwise evolution of the time-averaged film thickness, h_m, along the central axis of the channel, in the aerostatic case ($Re_g = 0$, empty circles) and with counter-current gas flow ($Re_g = 942$ ($u_g = 3.05\ \mathrm{m\ s^{-1}}$), filled circles). The horizontal dashed-line indicates the Nusselt thickness (flat-surface film thickness without gas flow) associated with the prescribed liquid Reynolds number. The opening slot through which ambient air is sucked spans from $x = 39$ cm to $x = 42$ cm (highlighted by vertical dot-dash lines). Here $Re_l = 35, f = 2.8$ Hz, $\eta_0 = 11$.

3. Results

Figure 6 displays shadowgraphs of the film surface and the corresponding spatiotemporal diagrams for different gas velocities at $Re_l = 35$ and $f = 2.8$ Hz. Increasing the gas velocity generates interactions between waves that can induce coalescence events, clearly visible in figure 6(f), resulting in solitary waves of high amplitude preceded by numerous capillary ripples in the downstream portion of the plane (figure 6c,e). The initial regular wavetrain is progressively disrupted by the counter-current gas flow as one moves downstream, but it remains globally 2-D before merging occurs. In this study, we are interested in this region of 2-D travelling waves, so measurements are performed at the location indicated by the white mark in figures 6(a), 6(c) and 6(e). In particular, we wish to know the nonlinear response of these waves to the strongly confined counter-current gas flow.

3.1. *Effect of confined counter-current gas flow on 2-D saturated travelling waves*

In this section, we confront the results obtained in our strongly confined channel with previous experiments conducted in a larger channel (Kofman *et al.* 2017). We consider a liquid film flowing at $Re_l = 35$ on which we force travelling waves of frequency $f = 2.8$ Hz through our coherent inlet forcing. We are interested in studying the effect of the counter-current gas flow on these waves, and, in particular, how this effect changes depending on the channel height.

Figure 7 confronts time records of the film thickness for the $H = 19$ mm channel (figure 7a–c), which corresponds to a relative confinement $\eta_0 = 39$ (Kofman *et al.* 2017), with those measured in our strongly confined $H = 5.2$ mm channel (figure 7d–f), where $\eta_0 = 11.1$. The measurement point was located at $x = 60$ cm from the liquid inlet in both experiments. Without imposed gas flow ($u_g = 0$, figure 7a,d) the wave train is identical in both cases, consisting of waves with a large-amplitude asymmetric hump preceded by three capillary ripples. Thus, the level of confinement is inconsequential for the

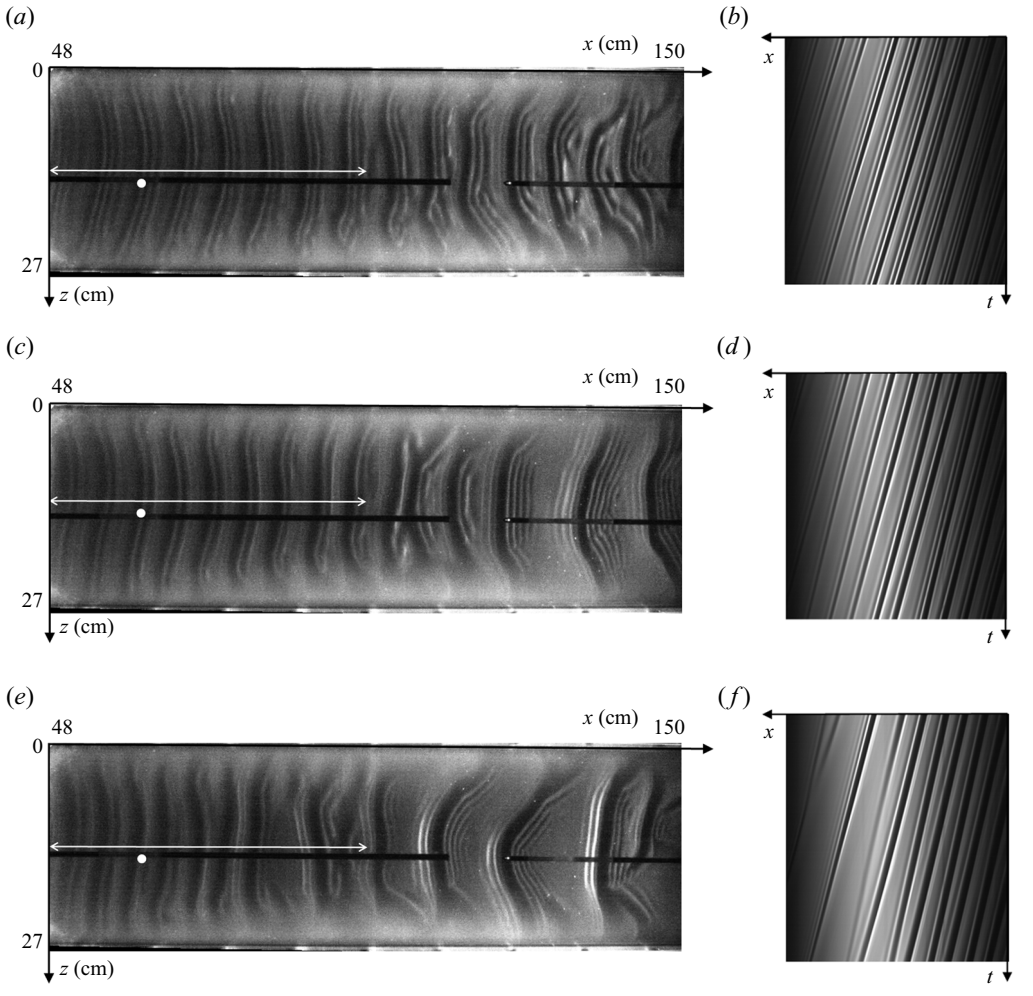

Figure 6. (*a*,*c*,*e*) Shadowgraphs of the gas–liquid interface over the entire test section for three different gas velocities, (*b*,*d*,*f*) associated spatiotemporal diagrams. Here (*a*,*b*) $u_g = 1.9$ m s^{-1} ($Re_g = 587$), (*c*,*d*) $u_g = 3.4$ m s^{-1} ($Re_g = 1023$), (*e*,*f*) $u_g = 4.1$ m s^{-1} ($Re_g = 1242$). These figures are the continuation of the aerostatic case ($u_g = 0$) presented in figure 4. The white dot and arrow are the same as those described in the caption of figure 4. Here $Re_l = 35$, $f = 2.8$ Hz, $\eta_0 = 11.1$.

aerostatic configuration. Starting from this reference state, we compare the response of solitary waves with a gradual increase of the gas velocity for both confinements (figure 7*b*,*e*,*c*,*f*). The striking difference between the two cases is that the maximum film height gradually increases with u_g in the large channel whereas it levels off in the strongly confined case. We also observe that the counter-current air flow attenuates the capillary ripples ahead of the main hump, as discussed in Kofman *et al.* (2017). This effect is much more pronounced in the strongly confined channel.

Figure 8 quantifies the gas effect on the wave characteristics for these two confinement levels. Figure 8(*a*) displays the effect of the gas on the wave velocity, c, and figure 8(*b*) its effect on the minimal (h_{min}), averaged (h_m) and maximal (h_{max}) values of the film thickness. We find that the slowing of the waves caused by the counter-current flow is more pronounced in the strongly confined channel than in the larger one. Figure 8(*b*) shows that

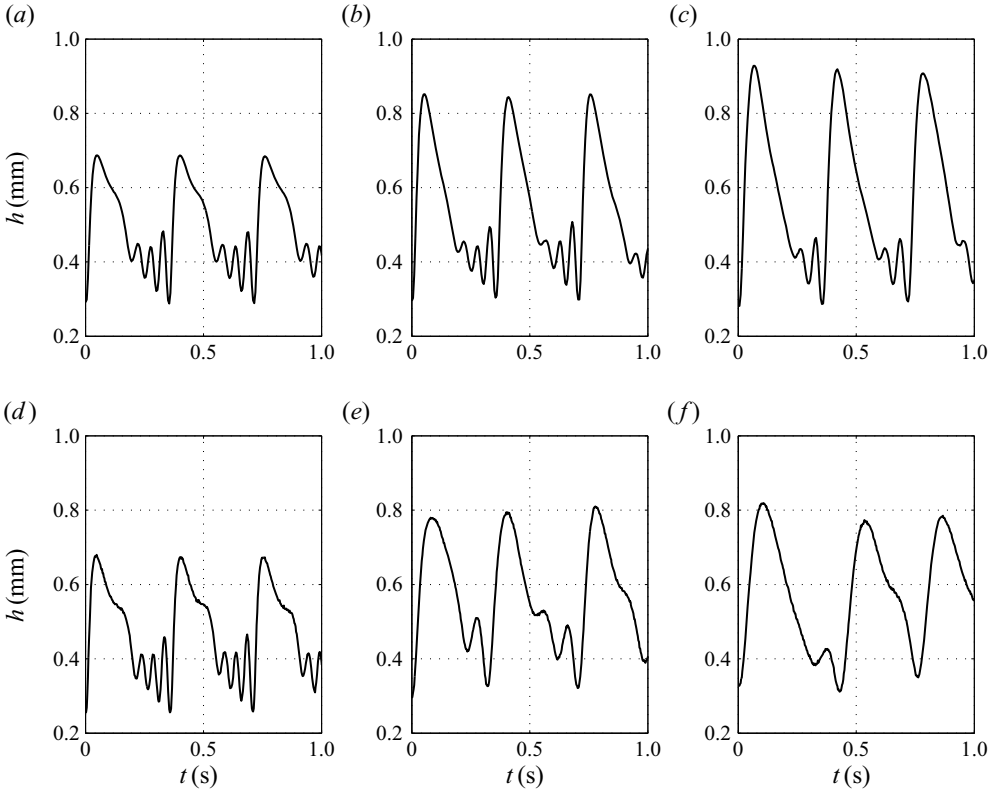

Figure 7. Influence of the gas velocity u_g on nonlinear wave profiles for two confinement levels: $\eta_0 = 39$ ($H = 19$ mm) and $\eta_0 = 11.1$ ($H = 5.2$ mm); $Re_l = 35$, $f = 2.8$ Hz, $x = 60$ cm. Here (*a*) $\eta_0 = 39$, $u_g = 0$ m s^{-1}; (*b*) $\eta_0 = 39$, $u_g = 3.3$ m s^{-1}; (*c*) $\eta_0 = 39$, $u_g = 4.4$ m s^{-1}; (*d*) $\eta_0 = 11.1$, $u_g = 0$ m s^{-1}; (*e*) $\eta_0 = 11.1$, $u_g = 3.4$ m s^{-1}; (*f*) $\eta_0 = 11.1$, $u_g = 4.4$ m s^{-1}.

h_{min} and h_{max} are influenced by the confinement. h_{min} slightly increases with u_g in the strongly confined channel while it remains constant in the large channel, or even slightly decreases for high gas velocities. As shown in figure 7, h_{max} in the strongly confined channel increases with u_g in a first stage ($u_g < 2.1$ m s^{-1} for $\eta_0 = 11.1$) then saturates, whereas it continuously increases in the large channel. By contrast, h_m increases by the same amount with u_g in all experiments, regardless of the confinement level. In order to account for this increase in the mean film thickness, we report in figure 9 the normalized quantities

$$\delta_{max} = \frac{h_{max}}{h_m} \tag{3.1}$$

based on the data from figure 8(*b*).

For $\eta_0 = 39$ ($H = 19$ mm), δ_{max} monotonously increases with u_g (open circles). Thus, increasing the gas flow rate amplifies the nonlinear waves, which implies a destabilizing (nonlinear) effect. This behaviour has been reported in several numerical studies (Trifonov 2010, 2019; Tseluiko & Kalliadasis 2011). By contrast, for the strongly confined channel, δ_{max} first increases but then clearly decreases with u_g (filled circles), in particular for $\eta_0 = 9.9$. These results confirm experimentally the numerical finding of Lavalle *et al.* (2021) that increasing the counter-current gas flow can attenuate nonlinear waves.

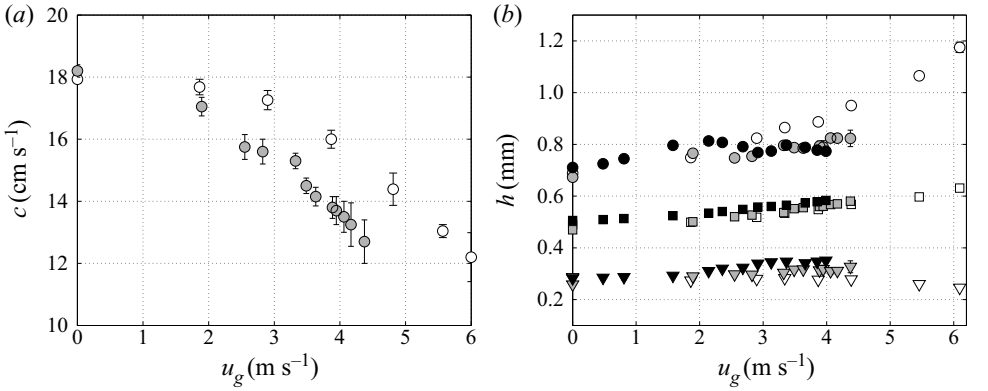

Figure 8. Influence of the gas velocity u_g on: (*a*) wave celerity c, (*b*) minimum h_{min} (downward triangles), mean h_m (squares) and maximum h_{max} (circles) film thickness for $\eta_0 = 39$, $\eta_0 = 11.1$ and $\eta_0 = 9.9$ (white, grey and black symbols, respectively). Here $Re_l = 35$, $f = 2.8$ Hz, $x = 60$ cm. Error bars are drawn for all symbols, but most of them are shorter than the symbol size in panel (*b*) and thus invisible.

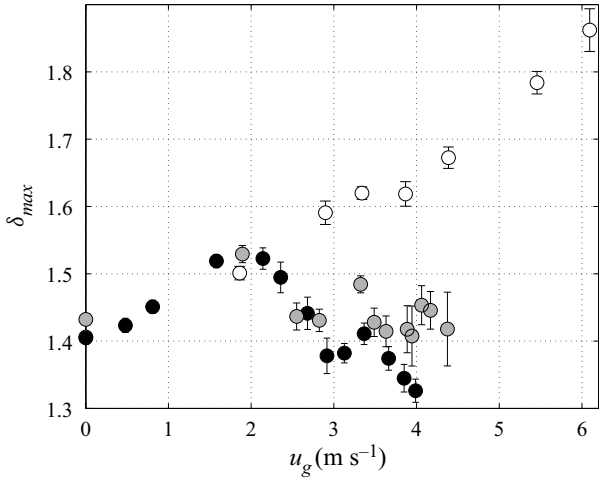

Figure 9. Influence of the gas velocity u_g on δ_{max} (3.1) for $\eta_0 = 39$, $\eta_0 = 11.1$ and $\eta_0 = 9.9$ (white, grey and black symbols, respectively). Here $Re_l = 35$, $f = 2.8$ Hz, $x = 60$ cm.

For the strongly confined channel, the attenuation of nonlinear waves observed in figure 9 sets in at $u_g > 2$ m s^{-1}. As shown in figure 8(*a*), this coincides with a sharp drop in wave celerity under the effect of the gas which is much more pronounced in the strongly confined channel than in the large channel. In figure 9, the wave amplitude curve $\delta_{max}(u_g)$ exhibits a saw-tooth shape during the stabilizing stage ($u_g > 2$ m s^{-1}) that will be discussed in the next subsection. For $\eta_0 = 11.1$ (grey symbols) the increase in $\delta_{max}(u_g)$ which reflects a redestabilization of the waves between $u_g = 2.9$ m s^{-1} and $u_g = 3.3$ m s^{-1} is correlated to the modulation in the wave celerity depicted in figure 8(*a*) (grey symbols) which means that the stabilization mechanism is very sensitive to the wave celerity.

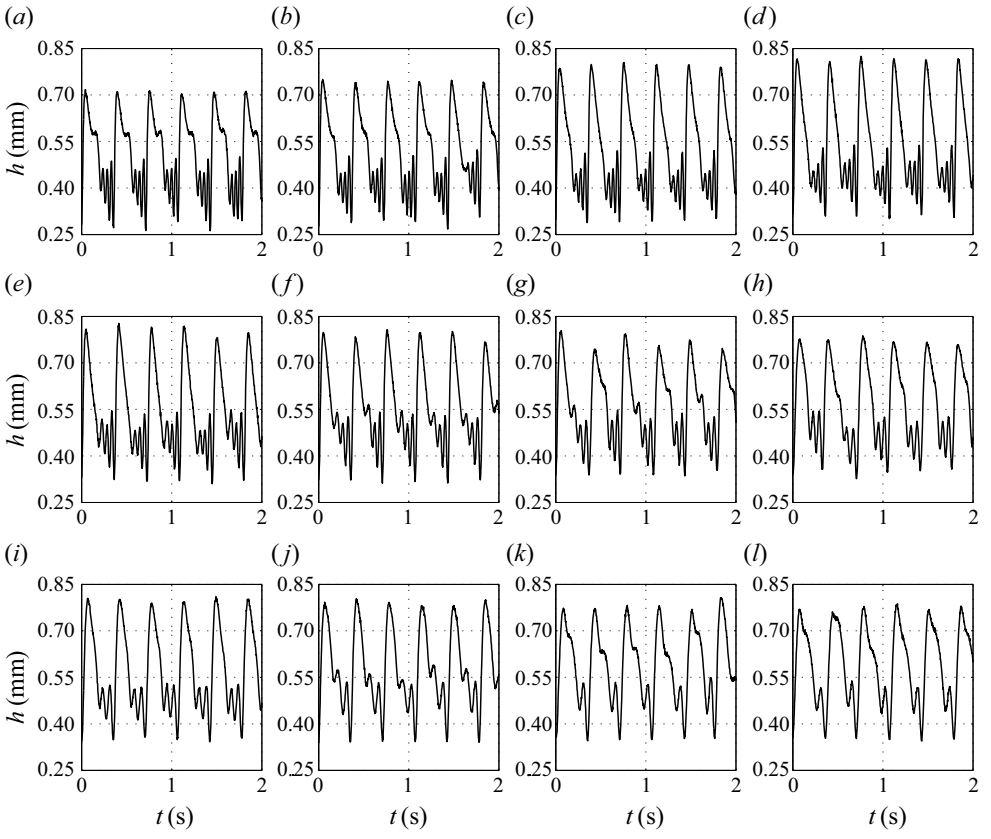

Figure 10. Influence of the gas velocity u_g on nonlinear wave profiles measured at $x = 60$ cm for $Re_l = 35$, $f = 2.8$ Hz, $\eta_0 = 9.9$, corresponding to the experiment presented in figure 9 (black symbols). Here (*a*) $u_g = 0$ m s^{-1}; (*b*) $u_g = 0.8$ m s^{-1}; (*c*) $u_g = 1.6$m s^{-1}; (*d*) $u_g = 2.1$ m s^{-1}; (*e*) $u_g = 2.4$ m s^{-1}; (*f*) $u_g = 2.7$ m s^{-1}; (*g*) $u_g = 2.9$ m s^{-1}; (*h*) $u_g = 3.1$ m s^{-1}; (*i*) $u_g = 3.4$ m s^{-1}; (*j*) $u_g = 3.7$ m s^{-1}; (*k*) $u_g = 3.8$ m s^{-1}; (*l*) $u_g = 4$ m s^{-1}.

3.2. *Effect of the counter-current gas flow on precursory capillary ripples*

The saw-tooth shape exhibited in figure 9 for the strongly confined channel at $u_g > 2.1$ m s^{-1} is correlated to the wave celerity and results in a sequential suppression of capillary ripples under the effect of an increasing gas flow, as shown in figure 10, where wave profiles at different gas velocities are displayed for $\eta_0 = 9.9$ (black symbols in figure 9). For $u_g < 2.1$ m s^{-1} the effect of the counter-current gas is to increase the wave amplitude without significantly affecting the wave speed and the number of capillary ripples remains unchanged (in this case, three capillary ripples are observed ahead of the main hump). For $u_g > 2.1$ m s^{-1}, the wave speed drops significantly, which reduces the wavelength of the main waves ($f = 2.8$ Hz is constant here). Both effects are known to reduce the number and amplitude of precursory capillary ripples (Dietze 2016), and this is observed in figure 10 ($\eta_0 = 9.9$): we move from three to two capillary ripples between $u_g = 2.9$ m s^{-1} (alternation of two or three capillary ripples) and $u_g = 3.1$ m s^{-1} (two capillary ripples) and from 2 to 1 at $u_g = 3.8$ m s^{-1} just before flooding. For $\eta_0 = 11.1$ (grey symbols in figure 9) the transition $3 \rightarrow 2$ and $2 \rightarrow 1$ occurs at $u_g \simeq 2.6$m s^{-1} and

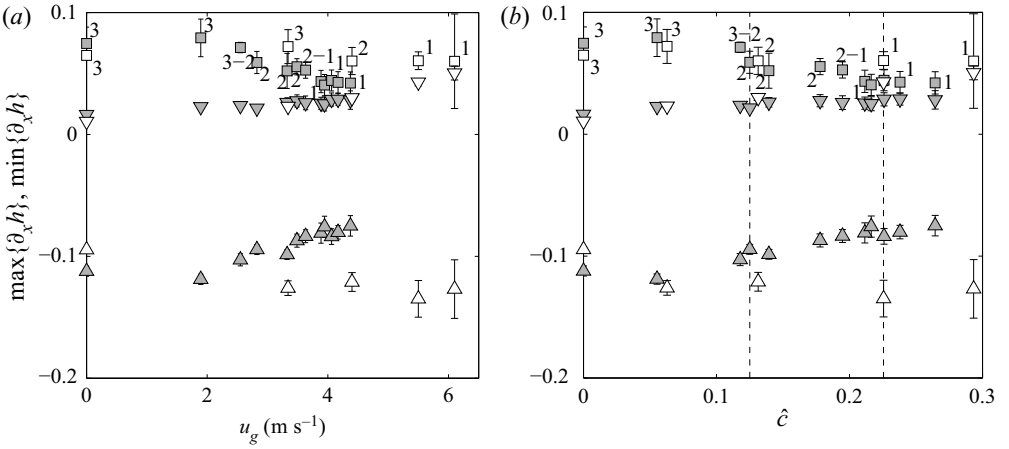

Figure 11. Influence of the gas velocity u_g in (a) and the normalized gas velocity $\hat{c}$ (3.2) in (b), on the maximum positive free-surface slope $\max\{\partial_x h\}$ at the back of the first capillary ripple (squares) and at the main hump tail (downward triangles), and on the maximum negative slope $\min\{\partial_x h\}$ at the front of the main hump (upward triangles), for $\eta_0 = 39$ (white symbols) and $\eta_0 = 11.1$ (grey symbols). The number of capillary ripples is indicated. Vertical dashed lines in (b) indicate the values of $\hat{c}$ related to the wave profiles presented in figure 12. Here $f = 2.8$ Hz, $Re_l = 35$, $x = 60$ cm.

3.6 m s^{-1}. The change in the number of capillary ripples correspond to the troughs of the saw-tooth shape in figure 9.

To confirm that the number of capillary ripples is indeed governed by the wave speed, figure 11 compares the maximum positive slope, $\max\{\partial_x h\}$, for the two confinement levels $\eta_0 = 11.1$ (grey symbols) and $\eta_0 = 39$ (white symbols). This maximum is observed at the back of the first capillary ripple (squares in figure 3b) and is an indicator of the compression of the capillary wave train due to the decrease of the wavelength. Figure 11(a) displays $\max\{\partial_x h\}$ (square symbols) as a function of u_g, and figure 11(b) as a function of the normalized wave velocity $\hat{c}$, i.e.

$$\hat{c} = \frac{c_0 - c}{c_N}, \tag{3.2}$$

where $c_N = g h_N^2 \sin\beta/\nu_l$ is the speed of kinematic waves in a passive atmosphere, c_0 corresponds to the measured wave speed in the case of a quiescent gas, and $h_N = (3\, q_l\, \nu_l/\sin\beta g)^{1/3}$ is the Nusselt thickness (the flat-surface film thickness in the passive-gas limit).

Figure 11(a) shows that for a given value of $u_g \neq 0$, the slope magnitude at the back of the first capillary ripple as well as the number of capillary ripples depend on the confinement. By contrast, figure 11(b) shows that for a given value of $\hat{c}$ these quantities are identical regardless of the confinement, which is also clearly visible from wave profiles presented in figure 12 for $\hat{c} = 0.13$ and $\hat{c} = 0.23$ (marked by vertical dashed lines in figure 11b). This behaviour implies that the capillary region is not directly affected by the gas shear-stress but is controlled by the indirect effect of the gas-induced slowing of the large waves. In figure 11 we have also plotted the maximum negative slope $\min\{\partial_x h\}$ at the main hump front (upward triangles) which is an indicator of the steepness of the wave, and the maximum (positive) slope at the wave tail (downward triangles). In the large channel (white symbols) the front inclination remains unchanged as the gas velocity is increased, while the tail steepens, thus resulting in a more symmetrical wave (thin solid

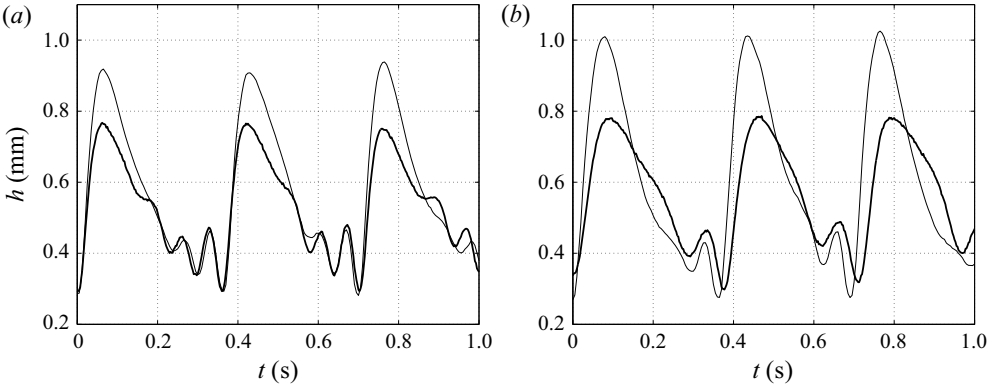

Figure 12. Influence of the confinement on wave profiles at given values of $\hat{c}$ (3.2) marked by vertical dashed lines in figure 11(*b*). Here (*a*) $\hat{c} = 0.13$; (*b*) $\hat{c} = 0.23$. Thin solid line, $\eta_0 = 39$ ($u_g = 4.4$ m s^{-1} in (*a*) and 5.5 m s^{-1} in (*b*)); thick solid line, $\eta_0 = 11.1$ ($u_g = 2.8$ m s^{-1} in (*a*) and 4 m s^{-1} in (*b*)). Same parameters as in figure 11.

curves in figure 12). By contrast in the strongly confined channel (grey symbols), the front inclination weakens while the tail slope remains unchanged under the action of the counter-current flow, and the resulting wave is less symmetric than in the large channel (thick solid curves in figure 12).

3.3. *Influence of the liquid Reynolds number*

We now investigate the effect of the counter-current gas flow on the response of nonlinear waves for different values of the liquid Reynolds number Re_l and the forcing frequency f, in the strongly confined channel. As shown in figure 13 for the quiescent-gas reference case, these parameters clearly affect the mean film thickness and consequently the confinement level η_0 (2.2), the maximum film thickness h_{max} and the number of precursory capillary ripples. The forcing frequency has been empirically adjusted from the aerostatic case according to the liquid Reynolds number, in order to generate 2-D saturated quasi-solitary waves in the working zone. The resulting wavelength of the unsheared wave train is specified in the caption of figure 13 provided that wave velocity measurements are available.

We report in figure 14 the variation of c (figure 14*a*) and δ_{max} (figure 14*b*) in terms of Re_g for different Re_l and forcing frequency f. For $Re_l = 44.6$ (grey triangles), we observe the same overall behaviour as for $Re_l = 35$, which was presented in the previous section. In a first stage, δ_{max} increases with Re_g (the gas flow is nonlinearly destabilizing) then decreases when c is significantly reduced (the gas flow is nonlinearly stabilizing), with saw-tooth modulations associated with the change in the number of capillary ripples, whereas the variation of c with Re_g remains monotonous. For a higher liquid flow rate, $Re_l = 49$ (crosses), the destabilizing stage at low gas velocity is replaced by a stabilizing one. For the lowest Reynolds number, $Re_l = 22$ (open triangles), there are only two capillary waves to start with (figure 13*a*) and we observe a weak stabilization until $Re_g \approx 600$, associated with the suppression of one capillary wave. Then δ_{max} increases to reach a constant value while maintaining one capillary wave until the experiment breaks down due to flooding downstream.

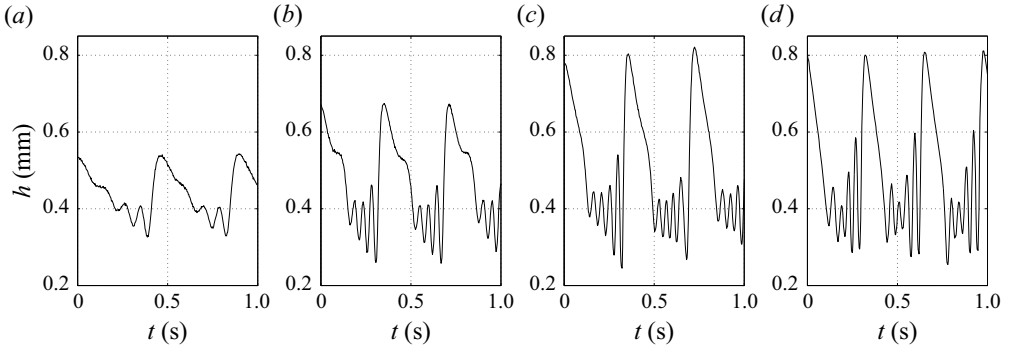

Figure 13. Wave profiles for different values of the liquid Reynolds number Re_l and forcing frequency f in the strongly confined channel for the aerostatic case. From left to right, the resulting wavelength is 6.5 cm ($Re_l = 22$), 6.5 cm ($Re_l = 35$), 7.3 cm ($Re_l = 44.6$), not available for $Re_l = 49$. Here (*a*) $R_l = 22, f = 2.2$ Hz, (*b*) $R_l = 35, f = 2.8$ Hz, (*c*) $R_l = 44.6, f = 2.8$ Hz, (*d*) $R_l = 49, f = 3.05$ Hz.

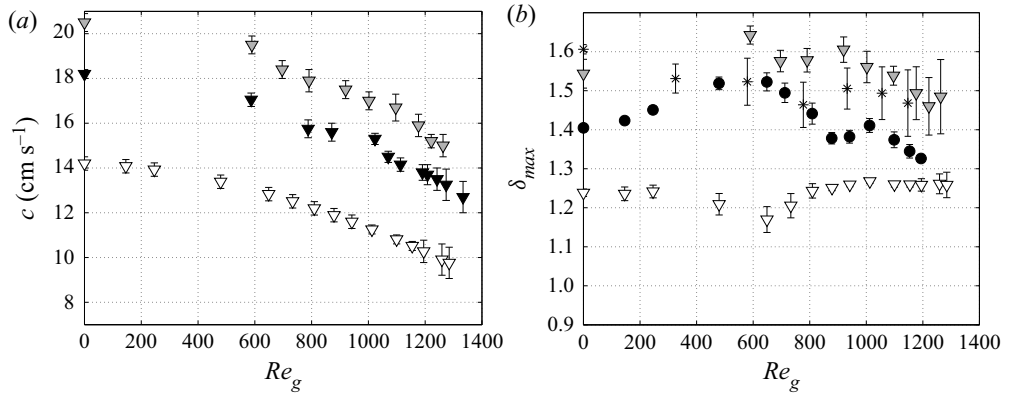

Figure 14. Influence of the liquid Reynolds number Re_l on: (*a*) wave celerity, $Re_l = 22$, $\eta_0 = 11.5$ (white triangles) – $Re_l = 35$, $\eta_0 = 11.1$ (black triangles) – $Re_l = 44.6$, $\eta_0 = 10.3$ (grey triangles); (*b*) $\delta_{max} = h_{max}/h_m$, same parameters as (*a*) for white and grey triangles, $Re_l = 35$, $\eta_0 = 9.9$ (black circles) – $Re_l = 49$, $\eta_0 = 10.3$ (crosses). strongly confined channel.

We now introduce the local relative confinement parameter η_{max} as

$$\eta_{max} = \frac{H}{h_{max}}. \tag{3.3}$$

Figure 15 displays η_{max} as a function of Re_g for the same parameters as figure 14. The gas-induced stabilization at $Re_l = 22$ is associated with a relative confinement $\eta_{max} \approx 9$. For $Re_l = 35$, 45 and 49 the stabilizing effect occurs for smaller confinement levels.

3.4. *Effect of the surface waves on the mean film thickness*

We now wish to gauge the effect of the gas-sheared surface waves on the mean film thickness h_m. In particular, we wish to know whether h_m is decreased or increased versus the primary-flow thickness. In the case of a passive gas or a quiescent unconfined atmosphere, it is well known that h_m is smaller than the primary-flow thickness. This is known as wave-induced effective film thinning (Miyara 1999). In our current case of a

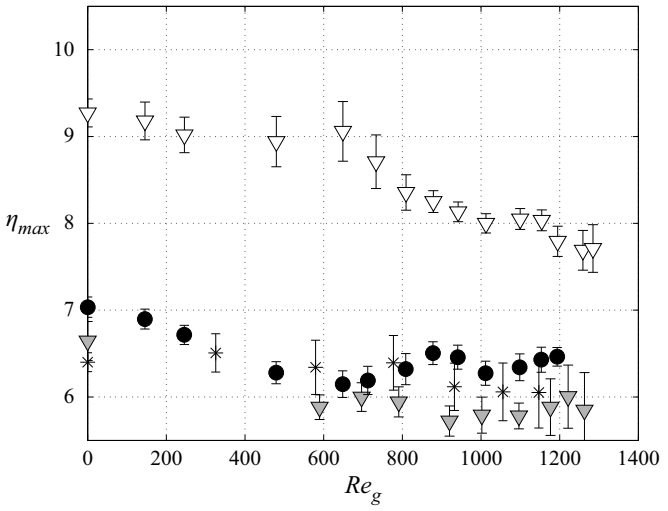

Figure 15. Influence of the liquid Reynolds number Re_l on the local confinement parameter η_{max} (3.3) in the strongly confined channel. Same parameters as in figure 14(*b*).

counter-current gas flow, it turns out that the wave effect depends on the confinement level. To group our measurement data for the $H = 5$ mm channel, where the gas flow is laminar, and the data of Kofman *et al.* (2017) for an $H = 19$ mm channel, where the gas flow is turbulent, we introduce the Froude number $Fr_{g,l}$, which relates interfacial shear stress ($\sim \rho_g u_g^2$) to gravitational effects,

$$Fr_{g,l} = \sqrt{\frac{\rho_g u_g^2}{\rho_l g \sin\beta h_N}}, \tag{3.4}$$

and the normalized film thickness $\hat{h}$, i.e.

$$\hat{h} = \frac{h_m}{h_m^0} - 1. \tag{3.5}$$

Figure 16(*a*) displays $\hat{h}$ as a function of $Fr_{g,l}$, for all experiments conducted in the $H = 5$ mm channel (different Re_l and f), as well as the experiments of Kofman *et al.* (2017) conducted in a $H = 19$ mm channel (square symbols). The experimental data collapse onto two different trends, one for the narrow channel and another for the wide channel. This is due to the different flow regimes in the two configurations, the gas flow being laminar in the former case and turbulent in the latter.

To account for this, we improve our approximation of the interfacial shear stress used in (3.4) in a modified gas–liquid Froude number, Fr_{fric}, based on the friction velocity, u_{fric}, as follows:

$$Fr_{fric} = \sqrt{\frac{\rho_g u_{fric}^2}{\rho_l g \sin\beta h_N}} = \sqrt{\frac{C_{f,i}}{2}} Fr_{g,l}, \tag{3.6}$$

where u_{fric} is based on the tangential interfacial gas shear stress of the primary flow (no waves), τ_i, as

$$u_{fric} = \sqrt{\frac{\tau_i}{\rho_g}}. \tag{3.7}$$

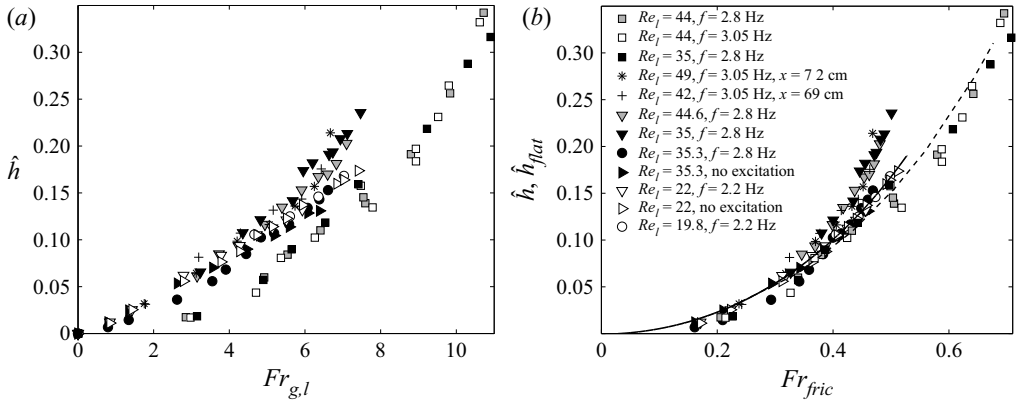

Figure 16. Relative mean film thickness $\hat{h}$ (3.5) measured in the $H \approx 5$ mm channel and in the $H \approx 19$ mm channel (Kofman *et al.* 2017, square symbols), as a function of: (*a*) the Froude number $Fr_{g,l}$ (3.4); (*b*) the modified Froude number, Fr_{fric} (3.6). The solid (laminar gas flow) and dashed (turbulent gas flow) curves correspond to the flat-film solution $\hat{h}_{flat}$ according to (B13) with $\epsilon = 0$ ($\hat{h}_{flat} = \tilde{h}_{flat} - 1$).

Here τ_i is related to the global skin-friction coefficient, $C_{f,i}$, as follows:

$$C_{f,i} = \frac{\tau_i}{1/2\rho_g u_g^2}. \tag{3.8}$$

In the strongly confined channel, the gas flow is laminar and we approximate $C_{f,i}$ by the relation for Poiseuille flow through a plane dry channel,

$$C_{f,i} = 12Re_g^{-1}. \tag{3.9}$$

In the large channel the gas flow is fully turbulent and we use an experimental correlation established by Patel & Head (1969) in a wide rectangular horizontal dry channel,

$$C_{f,i} = 0.0376Re_g^{-1/6}. \tag{3.10}$$

Using these correlations for $C_{f,i}$, we assume that the liquid–gas interface can be considered as immobile. To validate this motionless interface assumption, we have compared the film thickness of a flat-surface film subject with a counter-current laminar gas flow as obtained by numerical solution of the fully coupled two-phase primary flow (Lavalle *et al.* 2019) with the thickness obtained by assuming an interphase skin friction coefficient according to (3.9). Details on this flat-film model are given in Appendix B. The two predictions are in excellent agreement and this holds over the entire range of experimental conditions studied in this work (see figure 23 in Appendix B).

In figure 16(*b*), $\hat{h}$ (3.5) is plotted as a function of Fr_{fric}, according to (3.6). We observe that the new scaling is more appropriate to describe the effect of the shear stress exerted by the gas on the interface, as the laminar and turbulent data are now gathered. The two additional solid and dashed curves correspond to the flat-film model $\hat{h}_{flat}$ (according to (B13) with $\epsilon = 0$, $\hat{h}_{flat} = \tilde{h}_{flat} - 1$) for the laminar gas flow in the strongly confined channel (solid line) and for the turbulent gas flow in the large channel (dashed line). This model represents a reference solution for comparison with the wavy experimental data.

The mean film thickness results from two opposing intricate effects: the well-known effective thinning due to nonlinear surface waves, illustrated in figure 5 for the aerostatic case; and the thickening effect of the counter-current gas flow produced by the interfacial shear-stress. The relative competition of these two effects determines the mean film thickness ultimate behaviour.

In the large channel (square symbols) the experimental data lie slightly below the flat-film prediction. Thus, surface waves tend to reduce the mean film thickness, as in the case of a quiescent atmosphere.

In the strongly confined channel, at high liquid Reynolds number values Re_l and high Froude numbers ($Fr_{fric} \geqslant 0.35$), experimental data are clearly above the flat-film prediction which means that the mean wavy film thickness grows faster than the reference flat-film thickness. This behaviour occurs in the nonlinear stabilizing regime for strong relative confinement levels, where surface waves promote a significant variation of the gas cross-section, which in turn affects the local tangential shear stress. This is the basis for the linear stabilization mechanism described by Lavalle *et al.* (2019). In this regime, the gas effect tends to reduce the nonlinear amplitude of the main hump and thus the thinning effect of the waves, while it increases the residual flat film thickness between two humps. In figure 14(*b*), we observe that during this stage, the interaction between the liquid film and the counter-current gas flow generates strong disturbances of the wave train as highlighted by the large temporal fluctuations measurements for $Re_l = 44.6$ and 49.

By contrast, when Re_l and thus the wave amplitude is small, experimental data are well predicted by the flat-film model over the entire range of the Froude number. In this case, the mean thickness of the wavy film increases at the same rate as the flat film thickness when the gas flow rate is increased, indicating that the thinning effect of the surface waves balances the overall thickening effect due to the gas shear stress. This balance can also be observed at higher Re_l and moderate Froude number values ($Fr_{fric} \leqslant 0.35$, crosses) for experiments concerned with the monotonously nonlinear stabilizing regime (see crosses in figure 14*b*).

Further, we conclude that the interfacial shear stress effect on the nonlinear surface waves changes by increasing the gas velocity in the strongly confined channel. This behaviour could be related to the observations of Trifonov (2019), who performed simulations of nonlinear waves for a set of parameters similar to our experimental conditions ($\beta = 5^\circ$, $H = 5$ mm, $Re_l = 5$, 15 and 40, see the supplementary material associated with the cited article). The author demonstrates the existence of a local minimum of the mean film thickness and of the gas friction coefficient in terms of the gas superficial velocity. More specifically, at $Re_l = 40$, he found that the decrease of the friction coefficient deviates from the decreasing trend of the waveless solution ($\propto 1/Re_g$) at a gas velocity comparable to the experimental values associated with the deviation of h_m from the flat-film solution observed in figure 16(*b*).

The experimental data corresponding to the black filled circles deviates from the other data at similar liquid Reynolds numbers. For this experiment the Kapitza number is lower (by 13 % due to a different ambient temperature) and the channel height H is slightly lower (by 4 %). These variations do not significantly affect the primary flow, as can be inferred from the right-hand-pointing triangles which correspond to an experiment performed the same day without inlet forcing, and which lie on the solid curve related to the primary flow solution. However, the destabilizing effect of the gas on the nonlinear waves at moderate Froude number values may be enhanced, which could favour the wave-induced effective film thinning effect (these data lie below the solid curve).

4. Conclusion

In this paper, experiments were conducted on water films falling along the bottom wall of a weakly inclined ($\beta = 4.9^\circ$) rectangular channel of height $H \approx 5$ mm interacting with a laminar counter-current air flow. Surface waves were excited via coherent inlet forcing before they come into contact with the air flow to promote travelling waves consisting of a large-amplitude hump preceded by capillary ripples. We focused on the sheared region of the film where the waves were 2-D without interaction between them. Local film thickness time traces and wave celerity measurements have been performed together with visual observations.

The effect of the air flow on the height, shape and speed of the waves was investigated and contrasted with results obtained by Kofman *et al.* (2017) in a channel of height 19 mm, where the counter-current gas flow was turbulent. The stronger confinement level studied here versus the experiments of Kofman *et al.* (2017) not only changes the geometrical constriction of the gas flow but also leads to a laminar flow regime in the gas instead of a turbulent one. In experiments, these two effects, which play their own distinct roles, cannot be decoupled. However, Trifonov (2010) has shown via numerical simulations that the main effect of turbulence is to shift the onset of wave-induced critical events (e.g. the flooding onset) towards lower superficial gas velocities.

In our experiments, no confinement-induced effect was detected on the wave dynamics in the case of a quiescent gas. Indeed, the shape, amplitude and velocity of the nonlinear waves excited at a prescribed frequency are almost identical for the two confinement levels. When a counter-current gas flow is imposed, striking differences are observed. For all the experiments conducted in the weakly confined channel, the effect of the gas on the travelling nonlinear waves was destabilizing (see Kofman *et al.* 2017), whereas a monotonic stabilizing effect or a non-monotonic trend was observed in the strongly confined channel, depending on the liquid Reynolds number Re_l.

For small Re_l in the strongly confined channel, inertia is weak and the relative confinement is quite low without gas flow ($\eta_{max} > 9$). Under these conditions, the wave amplitude first slightly diminishes as the gas velocity is increased and then increases to reach a plateau sustaining one capillary ripple until onset of flooding. In that case, the stabilizing mechanism induced by the variation of the gas shear stress at the interface is quite weak.

For moderate Re_l, the wave amplitude first increases with the gas velocity while the number of capillary ripples ahead of the main hump and the wave celerity remain unchanged. Upon increasing the gas velocity further, the wave amplitude diminishes and a gradual reduction of the number of capillary ripples is observed. For higher values of Re_l, a monotonically gas-induced wave attenuation is observed.

These experimental observations are in line with recent numerical results obtained by Lavalle *et al.* (2021) in a superconfined channel, where monotonic gas-induced amplification (attenuation) of the nonlinear wave amplitude was detected for larger (smaller) H, and a non-monotonic trend was observed for intermediate H.

To quantify the effect of surface waves on the mean film thickness in a universal form, a modified Froude number has been constructed which relates viscous drag based on the skin friction coefficient and gravity. We have compared the normalized measured mean film thickness $\hat{h}$ with the primary-flow solution $\hat{h}_{flat}$ obtained in the limit of a frozen (immobile) liquid–gas interface. In the case of a turbulent gas flow, which corresponds to experiments conducted in the large channel, $\hat{h}_{flat}$ is greater than $\hat{h}$. In these experiments, waves are significantly amplified by the counter-current flow and the wave-induced film thinning effect (Miyara 1999) is dominant compared with the thickening effect of the gas

shear stress. In the laminar configuration, which corresponds to experiments conducted in the strongly confined channel, $\hat{h}$ and $\hat{h}_{flat}$ correspond when Re_l is small, which implies that the thinning effect of the waves on the mean thickness is balanced by the shear-stress thickening effect, and the experimental behaviour is well predicted by the model. For higher liquid Reynolds number values, $\hat{h}_{flat} < \hat{h}$ in the range of parameters where the nonlinear stabilization occurs.

Large-scale three-dimensional flow structures may arise in the gas flow and generate a non-zero spanwise tangential Reynolds/viscous stress at the liquid–gas interface. This stress may produce/enhance a spanwise variation of the film height and thus have a direct effect on the mean height $\hat{h}$ plotted in figure 16(*b*). Such an effect is not accounted for in Fr_{fric} (3.6), which is based on the streamwise tangential stress at the liquid–gas interface. In our current strongly confined experiments, where the gas flow is laminar, we can exclude a three-dimensional effect, as the wavefronts shown in figure 6 are quasi-2-D across the measurement range. In the weakly confined case of Kofman *et al.* (2017), where the gas flow is turbulent, wavefronts do display spanwise variations beyond a certain gas velocity (see figure 3 in that paper). Nonetheless, the corresponding data points in figure 16(*b*) are closely grouped. This either means that the effect of the spanwise component of the interfacial tangential gas shear stress on the film height is much weaker than that of the streamwise component for the studied conditions, or that the two effects are correlated.

Funding. This work was supported by the ANR WavyFilm project, grant ANR-15-CE06-0016-01 of the French Agence Nationale de la Recherche. The authors are grateful to J. Amrani, A. Aubertin, L. Auffray and R. Pidoux for their contribution to build the experimental set-up.

Declaration of interests. The authors report no conflict of interest.

Author ORCIDs.
Sophie Mergui https://orcid.org/0000-0002-9529-5133;
Gianluca Lavalle https://orcid.org/0000-0002-9866-5216;
Nicolas Grenier https://orcid.org/0000-0001-5436-7041;
Georg F. Dietze https://orcid.org/0000-0003-1495-5505.

Appendix A. Measurement of the gas flow rate

In this section we describe the procedure that has been used to quantify the air flow rate q_g generated by the fan in the inclined strongly confined channel of figure 1. This quantity is used to evaluate the gas Reynolds number according to (2.3). This was done based on a calibration curve between a given fan power and the corresponding gas flow rate obtained from velocity measurements in the dry channel, i.e. without the liquid film. The porous medium at the end of the bottom glass plate was replaced by a Plexiglas plate with an opening to allow access for a hot-wire anemometer probe (see figure 17). With this probe, we measured the wall-normal profile of the streamwise velocity $u(y)$ at the midwidth of the channel and 4.5 cm from the air inlet. Figure 18 displays profiles obtained for different fan powers and for the inclination angle used in the experiments, $\beta = 4.9°$. Each dot corresponds to a time-averaged measurement over 30 s and the error bars are included according to the uncertainty of the probe given by the manufacturer. A polynomial fit is performed for each profile from which we compute the air flow rate,

$$q_g = W \int_0^H u(y)\,\mathrm{d}y, \tag{A1}$$

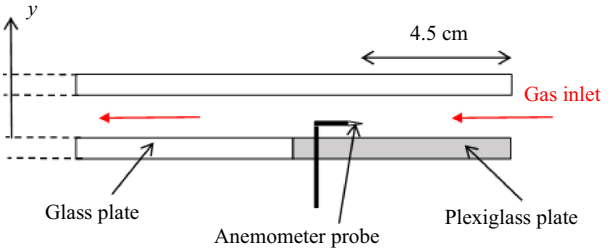

Figure 17. Location of the anemometer used to measure the air velocity at the end of the channel (gas inlet).

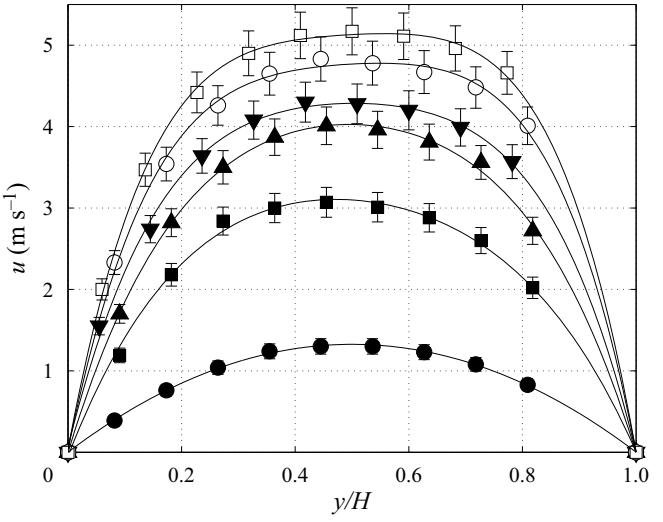

Figure 18. Air velocity profiles measured for different fan powers (in Watts) in the dry channel: $P_f = 1.3$ (circles); 3.9 (squares); 6.5 (upward triangles); 7.8 (downward triangles); 10.4 (open circles); and 13 (open squares). Solid lines correspond to polynomial fits. Here $\beta = 4.9^\circ$.

where $W = 27$ cm is the channel width. The calibration curve presented in figure 19 gives the air flow rate per unit width as a function of the imposed fan power, P_f. The gas Reynolds number, Re_g, is then calculated using (2.3). When the fan is switched off ($P_f = 0$), there is no gas flow in the dry channel, and, thus, $Re_g = 0$ according to our procedure, even though a small non-zero gas flow would be generated in the presence of a falling liquid film.

In figure 18, we have plotted several examples of measured velocity profiles for laminar flow conditions (black symbols), i.e. $Re_g < 1300$ according to the laminar–turbulent transition threshold determined by Patel & Head (1969) in a high-aspect-ratio channel. Table 1 reports the corresponding values of the velocity ratio u_g/u_{max}, where the mean velocity u_g has been defined in (2.4) and u_{max} is the maximum velocity. The aerodynamic entry length, L_d, is also reported, which is defined as the length needed for the boundary layers along the two horizontal channel walls to join at $y = H/2$. Based on the presumption that air enters the channel with a uniform velocity profile and using the Blasius correlation, it is straightforward to show that

$$\frac{L_d}{H} = 0.01 Re_g. \tag{A2}$$

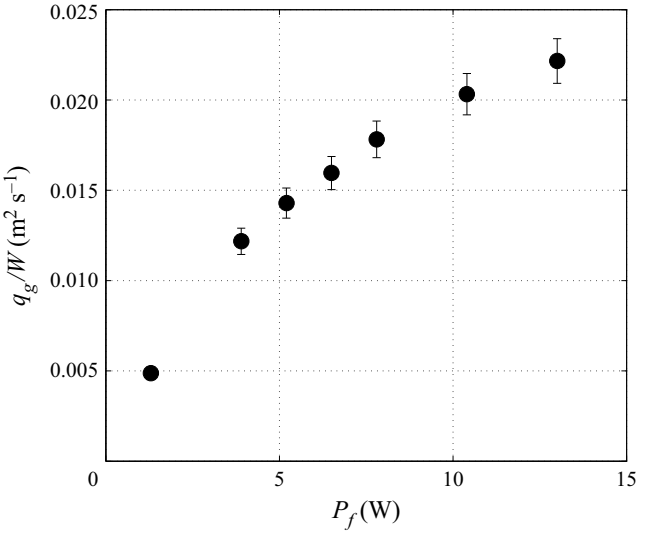

Figure 19. Calibration curve used to quantify the gas flow rate q_g (A1) per unit of channel width from the imposed fan power P_f. Here $\beta = 4.9^\circ$.

Re_g	u_g/u_{max}	L_d (mm)
325	0.667	17
810	0.721	42
1065	0.723	50
1190	0.757	55

Table 1. Ratio between the mean and the maximum air velocity issued from the measured velocity profiles (black symbols in figure 18) and the corresponding aerodynamic entry lengths given by (A2).

Based on this data, it is clear that the gas flow is fully developed in the entire region of the channel used for our falling liquid film experiments.

A specific velocity measurement series has been performed to confirm the laminar–turbulent transition threshold determined by Patel & Head (1969). The top glass plate of the channel was replaced by a Plexiglas plate with an opening to allow access for the probe far from the air entrance (approximately 1 m away). In this campaign, only the maximum air velocity, u_{max}, has been measured for different fan powers. By assuming that the flow is laminar and fully developed at this location, i.e. $u_g \approx 0.667 u_{max}$, we can calculate a flow rate and then a Reynolds number, Re_g^{lam}. For a given fan power, we compare Re_g^{lam} with Re_g issued from the complete vertical velocity profiles (using (A1) then (2.3)). Figure 20 displays Re_g^{lam} and Re_g against the imposed fan power. It can be seen that for $Re_g \leqslant 1200$ the points collapse, which means that $Re_g = Re_g^{lam}$ and thus the flow is confirmed to be laminar. The discrepancy observed for $Re_g > 1200$ means that the flow is no longer laminar. From these measurements we can conclude that in our inclined channel, the laminar–turbulent transition occurs for Re_g slightly greater than 1200.

The gas Reynolds number, Re_g, defined in (2.3) can be used to characterize the counter-current air flow in the experiments provided that the gas flow rate circulating into

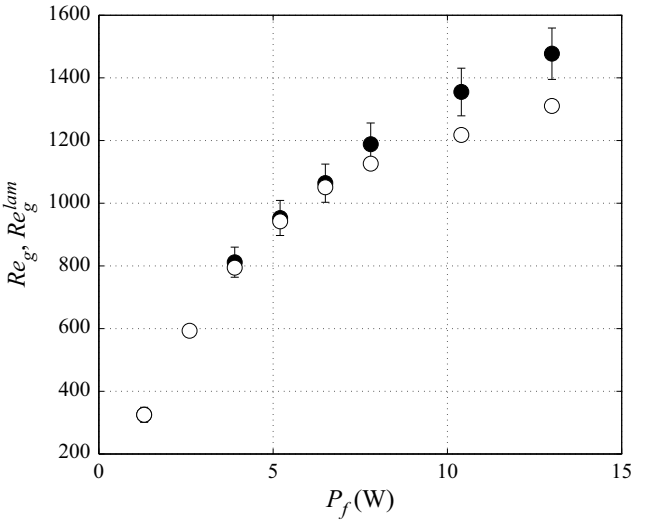

Figure 20. Here Re_g (filled circles) and Re_g^{lam} (open circles) as a function of the fan power P_f. Here Re_g is calculated by integrating velocity profiles measured at the end of the channel (figure 18), and Re_g^{lam} from the maximum velocity measurements performed in the fully developed region and assuming a laminar parabolic profile, i.e. $u_g = 2/3u_{max}$.

the experimental gas loop is not affected by the presence of the liquid film in the channel at a fixed fan power. The validity of this assumption is discussed below.

For a gas flowing in a dry rectangular channel with a large transversal aspect ratio of length L and height H (in our configuration $W/H = 54 \gg 1$), the pressure drop is given by the analytic relation $\Delta p_{channel} = 4C_f(L/2H)\frac{1}{2}\rho_g(q/H)^2$ where $q = u_g H$ is the volumetric gas flow rate (per unit width, i.e. $q = q_g/W$) and C_f is the skin friction coefficient, with $C_f = 12/Re_g$. Thus, $\Delta p_{channel} \propto q/H^3$ and the corresponding power $P_{channel} = q\Delta p_{channel} \propto q^2/H^3$. For a given power value $P_{channel}$, decreasing the channel height by 10 % (typical to the reduction due to the presence of the liquid film in the experiments) leads to a 15 % decrease in the flow rate. However, $\Delta p_{channel}$ constitutes only a small part of the total pressure drop, which is dominated by the resistance in the section between the outlet slot and the fan. Thus, the actual decrease in q_g upon decreasing H by 10 % is relatively low. For the range of parameters considered in this study, we have estimated it to be less than 5 %.

Appendix B. Flat-film model for laminar and turbulent gas flow

In figure 16(*b*), we have estimated the liquid film thickness of the flat-surface primary flow based on the skin friction coefficient $C_{f,i}$. This approach allows us to account for a laminar or turbulent gas flow within the flat-film model. For laminar flow, this coefficient $C_{f,i}$ is given by (3.9) and for turbulent flow by (3.10), according to the experiments of Patel & Head (1969). However, these experiments were performed in a dry channel, and, thus, our flat-film model implies an immobile liquid–gas interface. The current appendix aims to verify this assumption. We do this based on the laminar case, which is the limiting one, and for which we can easily obtain a reference solution for the flat-surface film based on the fully coupled primary flow (Lavalle *et al.* 2019).

The gas velocity profile for the fully coupled primary flow is given by

$$u(Y) = \frac{-K_g}{2\mu_g} H_g^2 \left(Y - Y^2\right) + u_0 \left(1 - Y\right), \tag{B1}$$

where K_g reads

$$K_g = \left(\partial_x p - \rho_g g \sin\beta\right), \tag{B2}$$

where $\partial_x p$ is the driving longitudinal pressure gradient, positive in our case for a counter-current gas flow, and $Y = (y - h_{flat})/H_g$, with h_{flat} denoting the flat-surface film thickness and $H_g = H - h_{flat}$ the height of the gas cross-section. Here u_0 is the liquid velocity at the film surface ($u_0 > 0$).

The gas velocity averaged over H_g can be written as

$$u_g^+ = \frac{-K_g}{12\mu_g} H_g^2 + \frac{u_0}{2} = u_g^0 + \frac{u_0}{2} = u_g^0 \left(1 + \frac{\epsilon}{2}\right), \tag{B3}$$

where u_g^0 corresponds to the average gas velocity in the limit $u_0 = 0$ and $\epsilon = u_0/u_g^0$.

The gas Reynolds number is defined as

$$Re_g^+ = \frac{u_g^+ H_g}{\nu_g} = \frac{u_g^0 H_g}{\nu_g} + \frac{u_0 H_g}{2\nu_g} = Re_g^0 + Re_0 = Re_g^0 \left(1 + \frac{\epsilon}{2}\right). \tag{B4}$$

We can write the tangential shear-stress at the liquid–gas interface and at the top wall, τ_i and τ_w, as

$$\tau_i = -\frac{\mu_g}{H_g} \partial_Y u|_{Y=0} = \frac{K_g}{2} H_g + \mu_g \frac{u_0}{H_g} = \tau_i^0 \left(1 - \frac{\epsilon}{6}\right), \tag{B5}$$

$$\tau_w = \frac{\mu_g}{H_g} \partial_Y u|_{Y=1} = \frac{K_g}{2} H_g - \mu_g \frac{u_0}{H_g} = \tau_i^0 \left(1 + \frac{\epsilon}{6}\right), \tag{B6}$$

where $\tau_i^0 = H_g K_g/2$ is the limit of τ_i and τ_w for a static interface (i.e. for $\epsilon = 0$).

We define the global skin-friction coefficient at the liquid–gas interface, $C_{f,i}$ as

$$\begin{aligned} C_{f,i} &= \frac{\tau_i}{1/2\rho_g u_g^{+2}} \\ &= \frac{\tau_i^0}{1/2\rho_g u_g^{0^2}} \frac{1 - \epsilon/6}{(1 + \epsilon/2)^2} = C_{f,i}^0 \frac{1 - \epsilon/6}{(1 + \epsilon/2)^2}. \end{aligned} \tag{B7}$$

In a similar way we can define $C_{f,w}$ at the top wall as

$$C_{f,w} = C_{f,i}^0 \frac{1 + \epsilon/6}{(1 + \epsilon/2)^2}, \tag{B8}$$

where $C_{f,i}^0$ is the skin friction coefficient in the case of static boundaries (i.e. for $\epsilon = 0$). In the case of a laminar gas flow, it is given by

$$C_{f,i}^0 = \frac{-12}{Re_g^0}. \tag{B9}$$

For convenience, in the experiments u_g is always taken as positive, therefore $u_g = -u_g^0$ and $Re_g = -Re_g^0$ in our counter-current case.

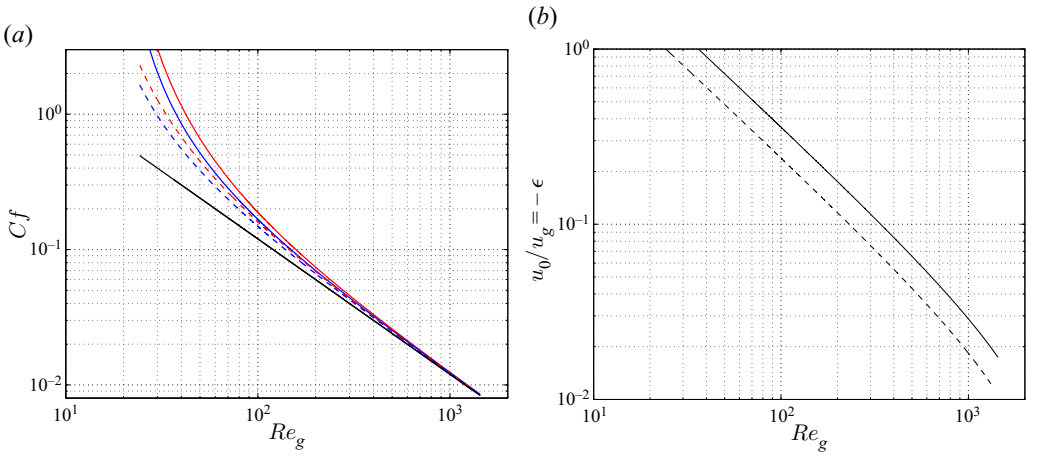

Figure 21. (*a*) Global skin-friction coefficients at the liquid–gas interface $C_{f,i}$ (B7) (red line) and at the upper wall of the channel $C_{f,w}$ (B8) (blue line) as a function of Re_g, calculated from the fully coupled primary flow solution. The black line corresponds to a skin-friction coefficient in the case of a static interface (i.e. $\epsilon = 0$). (b) Ratio between the interface velocity and the gas velocity $u_0/u_g = -\epsilon$. $Re_l = 22$ (dashed lines) and $Re_l = 44.6$ (solid lines), $\beta = 4.9^\circ$, $H = 5.2$ mm.

Now, we compute $C_{f,i}$ and $C_{f,w}$ based on (B7) and (B8), using the liquid velocity at the interface u_0 (which enters ϵ) from the fully coupled primary-flow solution. Figure 21(*a*) displays $C_{f,i}$ (red lines), $C_{f,w}$ (blue lines) and $C^0_{f,i}$ (black line) as a function of the gas Reynolds number $Re_g = -Re^0_g$ over the range $25 < Re_g < 1500$, for two liquid Reynolds numbers considered in our experiments with $H = 5.2$ mm: $Re_l = 22$ (dashed lines) and $Re_l = 44.6$ (solid lines). The associated variation of $u_0/u_g = -\epsilon$ is presented in figure 21(*b*). To specify the range of parameters where the static interface approximation based on the skin-friction coefficient criteria can be considered as valid, we focus on the gas Reynolds values such as the difference between $C_{f,i}$ and $C^0_{f,i}$ is less than 10 %. From figure 21(*a*) we can conclude that this criterion is met for $Re_g > 250$ ($Re_l = 22$) and $Re_g > 400$ ($Re_l = 44.6$), which corresponds to $u_0/u_g \leqslant 0.08$ in figure 21(*b*). Figure 21(*a*) also shows that $C_{f,i} \approx C_{f,w}$ over a range of u_0/u_g where the static interface assumption is no longer valid. For example, the discrepancy between $C_{f,i}$ and $C_{f,w}$ is around 10 % in figure 21(*a*) for $(Re_l, Re_g) = (22, 80)$ and $(44.6, 125)$, corresponding to $u_0/u_g \approx 0.3$ in figure 21(*b*). This behaviour can be explained by the change in the gas velocity distribution with the gas flow rate. Indeed, the location of the maximum gas velocity is shifted towards the top wall when u_0/u_g is increased by decreasing Re_g, as shown in figure 22. Consequently, the tangential shear stress is reduced at the liquid–gas interface while it increases at the top wall and the dissymmetry arising from the moving interface is partially attenuated.

To go further in testing the validity of this frozen-interface approximation, we will compare the film thickness obtained from the fully coupled primary flow solution with the thickness obtained by assuming an interphase skin friction coefficient according to (B9) using a simple model described below.

We start by writing the velocity profile in the liquid film as

$$u_l(y) = \frac{K_l}{\mu_l}\left(h_{flat}y - \frac{y^2}{2}\right) - \frac{\tau_i}{\mu_l}y. \tag{B10}$$

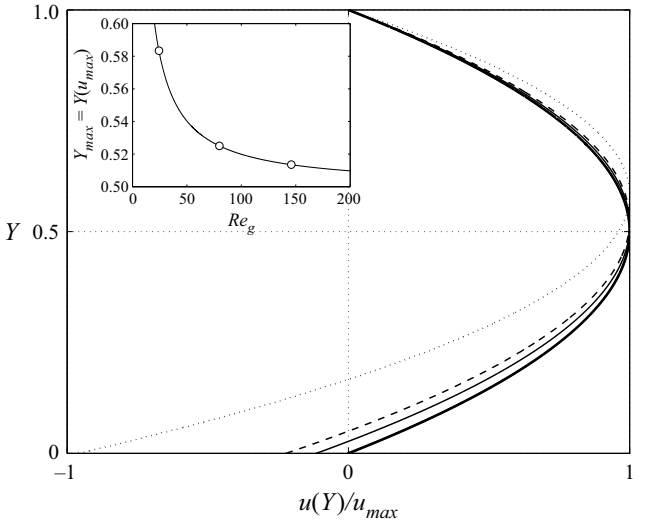

Figure 22. Gas velocity profiles calculated from the fully coupled primary flow solution for $Re_l = 22$: $u(Y)/u_{max}$ with $u(Y)$ according to (B1) and $u_{max} = \min(u(Y)) < 0$. Dash–dot line, $u_0/u_g = 1$ ($Re_g = 24.3$); dashed line, $u_0/u_g = 0.3$ ($Re_g = 80$); solid line, $u_0/u_g = 0.16$ ($Re_g = 145$); thick solid line, $u_0 = 0$ (Poiseuille flow). The location of u_{max} in the channel, $Y_{max} = Y(u_{max})$, is plotted in the inset as a function of Re_g ($Y_{max} = 0.5$ for a Poiseuille flow). Open circles mark Y_{max} for the profiles represented in the figure (except the Poiseuille flow). Here $\beta = 4.9°$, $H = 5.2$ mm.

Here K_l reads as

$$K_l = \left((\rho_l - \rho_g) g \sin\beta - \frac{\tau_i + \tau_w}{H - h_{flat}} \right), \tag{B11}$$

where τ_i and τ_w are given by (B5) and (B6), respectively. Therefore, $\tau_i + \tau_w = 2\tau_i^0 = \rho_g u_g^{0^2} C_{f,i}^0 = \rho_g u_g^2 C_{f,i}^0$.

Integrating (B10) across the liquid layer gives the liquid flow rate

$$Q_l = \frac{K_l}{3\mu_l} h_{flat}^3 - \frac{\tau_i}{2\mu_l} h_{flat}^2. \tag{B12}$$

By expressing the flow rate $Q_l = (\rho_l g \sin\beta)(3\mu_l)^{-1} h_N^3$ in terms of the Nusselt thickness h_N, i.e. the thickness of an equivalent fully developed flat-surface film falling in a passive atmosphere, we obtain the following equation for the flat-surface film thickness sheared by a counter-current gas flow,

$$\left(1 - \frac{\rho_g}{\rho_l} - \underbrace{Fr_{g,l}^2 C_{f,i}^0 \left(\frac{H}{h_N} - \tilde{h}_{flat} \right)^{-1}}_{\Lambda_p} \right) \tilde{h}_{flat}^3 - \underbrace{\frac{3}{4} Fr_{g,l}^2 C_{f,i}^0 (1 - \epsilon/6) \tilde{h}_{flat}^2}_{\Lambda_i} - 1 = 0, \tag{B13}$$

where $\tilde{h}_{flat} = h_{flat}/h_N$. The contribution of pressure gradient in the gas phase is included in Λ_p and the contribution of the interfacial shear-stress is included in Λ_i. The interphase skin friction coefficient $C_{f,i}^0$ is given by (B9) in the laminar case and $Fr_{g,l}$ is given by (3.4).

The contribution of the moving interface is represented by $\epsilon = u_0/u_g^0$, the ratio between the interface velocity and the gas velocity ($\epsilon < 0$ in our counter-current case). By assuming

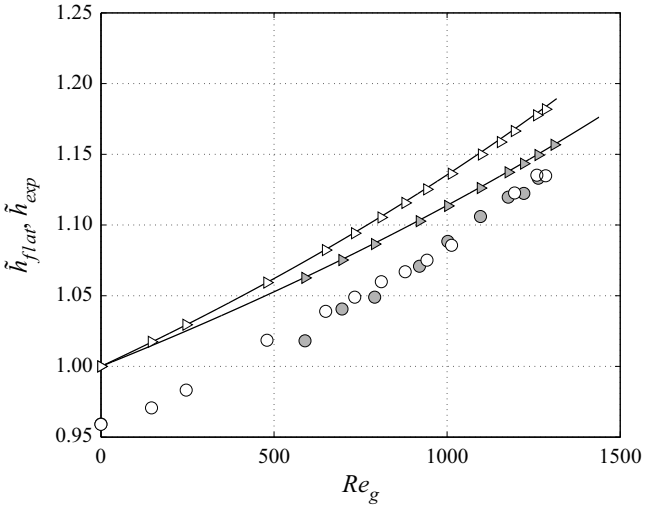

Figure 23. Thickness of a flat-surface film (normalized by the Nusselt thickness h_N) subject to a counter-current laminar gas flow, obtained from the flat-film model (triangles) (according to (B13) with $\epsilon = 0$) compared with the numerical solution of the fully coupled two-phase primary flow (solid lines). The normalized mean film thickness $\tilde{h}_{exp} = h_m/h_N$ measured in the experiments is also reported (circles). Here $Re_l = 22$ (white symbols) and $Re_l = 44.6$ (grey symbols), $\beta = 4.9^\circ$, $H = 5.2$ mm.

$\epsilon = 0$, i.e. the liquid–gas interface is static, the liquid and gas phases are coupled only via the interface position h_{flat}.

In figure 23, we compare the solution given by the model from solving (B13) assuming $\epsilon = 0$ (symbols) with the film thickness obtained from solving the fully coupled two-phase primary flow (solid lines), for $Re_l = 22$ and $Re_l = 44.6$, and for gas Reynolds number values according to the experiments. The results obtained from these two approaches are in excellent agreement over the entire range of experimental conditions, even for small gas Reynolds numbers for which $|\epsilon|$ is not so small. Indeed, if we go back for example to the aforementioned experiment conducted with $Re_l = 22$ and $Re_g = 145$, $\epsilon = -0.3$ (see figure 21*b*) which implies that the effect of the interfacial shear stress (Λ_i in (B13)) is underestimated by only $0.3/6 = 5\,\%$ by assuming an immobile liquid–gas interface. From this analysis, we can conclude that this approximation is admissible in all the experiments presented in the current paper.

Finally, the normalized mean film thickness $\tilde{h}_{exp} = h_m/h_N$ measured in the experiments is also reported in figure 23, for $Re_l = 22$ and $Re_l = 44.6$. We observe that $\tilde{h}_{exp} < \tilde{h}_{flat}$ reflecting the effective film thinning due to the presence of interfacial waves in experiments. For $Re_l = 22$, $\tilde{h}_{exp}$ increases in the same amount as $\tilde{h}_{flat}$ when the gas flow is increased, whereas $\tilde{h}_{exp}$ increases faster than $\tilde{h}_{flat}$ for $Re_l = 44.6$. This behaviour is discussed in § 3.3.

References

ALEKSEENKO, S.V., AKTERSHEV, S.P., CHERDANTSEV, A.V., KHARLAMOV, S.M. & MARKOVICH, D.M. 2009 Primary instabiliies of liquid film flow sheared by turbulent gas stream. *Intl J. Multiphase Flow* **35**, 617–627.

BENJAMIN, T.B. 1957 Wave formation in laminar flow down an inclined plane. *J. Fluid Mech.* **2**, 554–574.

COHEN-SABBAN, J., GAILLARD-GROLEAS, J. & CREPIN, P.-J. 2001 Quasi-confocal extended field surface sensing. In *Proccedings of SPIE, Optical Metrology Roadmap for Semiconductor, Optical, and Data Storage Industries II* (ed. A. Duparre & B. Singh), vol. 4449, pp. 178–183. Society of Photo-optical Instrumentation Engineers.

DIETZE, G.F. 2016 On the Kapitza instability and the generation of capillary waves. *J. Fluid Mech.* **789**, 368–401.

DIETZE, G.F. & RUYER-QUIL, C. 2013 Wavy liquid films in interaction with a confined laminar gas flow. *J. Fluid Mech.* **722**, 348–393.

DROSOS, E.I.P., PARAS, S.V. & KARABELAS, A.J. 2006 Counter-current gas–liquid flow in a vertical narrow channel – liquid film characteristics and flooding phenomena. *Intl J. Multiphase Flow* **32** (1), 51–81.

KAPITZA, P.L. 1948 Wave flow of a thin viscous fluid layers. *Zh. Eksp. Teor. Fiz.* **18**(1), 3–28.

KOFMAN, N., MERGUI, S. & RUYER-QUIL, C. 2017 Characteristics of solitary waves on a falling liquid film sheared by a turbulent counter-current gas flow. *Intl J. Multiphase Flow* **95**, 22–34.

KUSHNIR, R., BARMAK, I., ULLMANNL, A. & BRAUNER, N. 2021 Stability of gravity-driven thin-film flow in presence of an adjacent gas phase. *Intl J. Multiphase Flow* **135**, 103443.

LAVALLE, G., GRENIER, N., MERGUI, S. & DIETZE, G.F. 2020 Solitary waves on superconfined falling liquid films. *Phys. Rev. Fluids* **5** (3), 032001(R).

LAVALLE, G., LI, Y., MERGUI, S., GRENIER, N. & DIETZE, G.F. 2019 Suppression of the Kapitza instability in confined falling liquid films. *J. Fluid Mech.* **860**, 608–639.

LAVALLE, G., MERGUI, S., GRENIER, N. & DIETZE, G. 2021 Superconfined falling liquid films: linear versus nonlinear dynamics. *J. Fluid Mech.* **919**, R2.

LIU, J. & GOLLUB, J.P. 1994 Solitary wave dynamics of film flows. *Phys. Fluids* **6** (5), 1702–1712.

LIU, J., PAUL, J.D. & GOLLUB, J.P. 1993 Measurements of the primary instabilities of film flows. *J. Fluid Mech.* **250**, 69–101.

MIYARA, A. 1999 Numerical analysis on flow dynamics and heat transfer of falling liquid films with interfacial waves. *Heat Mass Transfer* **35**, 298–306.

PATEL, V.C. & HEAD, M.R. 1969 Some observations on skin friction and velocity profiles in fully developed pipe and channel flows. *J. Fluid Mech.* **38** (1), 181–201.

TILLEY, B.S., DAVIS, S.H. & BANKOFF, S.G. 1994 Nonlinear long-wave stability of superposed fluids in an inclined channel. *J. Fluid Mech.* **277**, 55–83.

TRIFONOV, Y.Y. 2010 Counter-current gas-liquid wavy film flow between the vertical plates analyzed using the Navier–Stokes equations. *AIChE J.* **56** (8), 1975–1987.

TRIFONOV, Y.Y. 2017 Instabilities of a gas-liquid flow between two inclined plates analyzed using the Navier–Stokes equations. *Intl J. Multiphase Flow* **95**, 144–154.

TRIFONOV, Y.Y. 2019 Nonlinear wavy regimes of a gas-liquid flow between two inclined plates analyzed using the Navier–Stokes equations. *Intl J. Multiphase Flow* **112**, 170–182.

TSELUIKO, D. & KALLIADASIS, S. 2011 Nonlinear waves in counter-current gas-liquid film flow. *J. Fluid Mech.* **673**, 19–59.

VALLURI, P., MATAR, O.K., HEWITT, G.F. & MENDES, M.A. 2005 Thin film flow over structured packings at moderate Reynolds numbers. *Chem. Engng Sci.* **60**, 1965–1975.

VELLINGIRI, R., TSELUIKO, D. & KALLIADASIS, S. 2015 Absolute and convective instabilities in counter-current gas–liquid film flows. *J. Fluid Mech.* **763**, 166–201.

VLACHOS, N.A., PARS, S.V., MOUZA, A.A. & KARABELAS, A.J. 2001 Visual observations of flooding in narrow rectangular channels. *Intl J. Multiphase Flow* **27**, 1415–1430.

YIH, C.S. 1963 Stability of liquid flow down an inclined plane. *Phys. Fluids* **6** (3), 321–334.

ZAPKE, A. & KRÖGER, D.G. 2000 Countercurrent gas-liquid flow in inclined and vertical ducts – I: flow patterns, pressure drop characteristics and flooding. *Intl J. Multiphase Flow* **26**, 1439–1455.